



Digital Holographic Microscopy for MEMS/MOEMS Device Inspection and Complete Characterization

G.M. Hegde^{a*}, Vijay Raj Singh^b and Anand Asundi^b

Abstract | Digital holography became feasible since the availability of charged coupled devices (CCDs) with smaller pixel sizes, higher pixel numbers and high speed computers. Fresnel or Fourier holograms are recorded directly by the CCD and stored digitally in the computer. The reconstruction of the wavefield, which is done optically by illumination of a hologram in conventional holography, is performed by numerical methods in digital holography. In the numerical reconstruction process, not only the intensity but also the phase distribution of the stored wavefield can be computed from the digital hologram. This offers new possibilities for a variety of applications. This review article describes the principle of digital holographic microscopy (DHM) and its major applications in microelectro-optomechanical systems (MEMS/MEOMS) inspection and characterization. MEMS structures are generally realized using different material layers involving various process steps. Static and dynamic characterization of MEMS devices form an important part in carrying out their functional testing and reliability analyses. Development of a digital holography (DH) based system for micro-device inspection and characterization is presented in this review. A reflection mode hand-held type compact DH microscope system is developed based on the lensless magnification configuration. Application of the developed system is demonstrated for MEMS structures such as cantilever, diaphragms, accelerometer, micro-heater inspection. Further, both static and dynamic characterizations of these MEMS structures are illustrated.

Keywords: digital holographic microscopy, MEMS characterization, static, dynamic characterization.

1 Introduction

Optical metrology has many advantages over other measurement techniques because of its non-invasive, high sensitivity, large temporal and spatial resolution features. Various optical methods are being used for imaging and measurement applications. The miniaturization of the object/device size puts new challenges for optical metrology. Some examples are dynamic microscopic imaging, and measurements on micro-structures (MEMS/MEOMS devices). The requirements are better measurement system

performance for full 3D, large field of view and high imaging resolution as well as real time analysis. Holography is an important tool for optical metrology. Dennis Gabor invented holography in 1948 as a two-step lensless imaging process for wavefront reconstruction.¹ The phase, amplitude, polarization, and coherence of a wave field can be stored in a hologram during recording. Since these quantities cannot be measured directly with conventional detectors, which are only sensitive to the intensity, this makes the holographic technique most attractive. In classical holography,

^aCentre for Nano Science and Engineering, Indian Institute of Science, Bangalore 560012, India.

^bSchool of Mechanical and Aerospace Engineering, Nanyang Technological University, Nanyang Avenue, Singapore 639798.

*nanogopal@cense.iisc.ernet.in

photographic plates or thermoplastic films are used to record holograms in vibration free environment and then optically reconstructed. The handling of these materials is time consuming and the vibration isolation requirement makes holographic technique less popular to implement in industrial environment. With the recent development in fast computers and high resolution charged coupled devices (CCD), digital holography (DH)² is expected to overcome the problems of classical holography and also enhance its utility in real time imaging and processing of the holograms. Digital recording devices (CCD sensor) provide flexibility to record holograms directly in digital form at video rate. The reconstruction process is then performed numerically giving quantitative analysis of amplitude and phase of the wavefront.³⁻⁶ This offers new possibilities for a variety of applications, which in classical holography was done only qualitatively. Over the past decade there has been an enormous progress in DH systems development and methodologies for wide range of applications.⁷⁻¹⁸ DHM is digital holography applied to microscopy. DHM distinguishes itself from other microscopy techniques by not recording the projected image (contains only single axial plane information) of the object, instead recording the light wave front information (contains entire 3D information) originating from the object and digitally recorded as a hologram. Later the object 3D image is reconstructed on the computer by using a numerical reconstruction algorithm.¹⁹⁻²¹ The image forming lens in traditional optical microscopy is replaced by a computer algorithm without any mechanical scanning used for 3D imaging.

Integration of mechanical elements, electronics, optical components, and actuators on a common silicon substrate using micromachining technology constitute microelectro-optomechanical systems (MEOMS).²² It has a wide range of applications in scientific and engineering fields. MEMS devices are generally realized using different material layers with different properties involving various fabrication processes that often involve chemical/plasma etching, high temperature and other chemical treatments. Consequently, their final shape, structural integrity and performance are affected by the presence of residual stresses, appearing in the form of undesired in-plane and out-of-plane deformations. Hence, characterization of the mechanical properties such as geometrical imperfections inherent to the process, stress gradient effects, deformations, real boundary conditions and damping mechanisms of MEMS structures at different stages of manufacturing process is very significant

from the fabrication process and device performance points of view. Further, it is very important to study MEMS devices subjected to vibrations. The purpose of dynamic MEMS testing is to provide feedback about device behavior, system parameters, and material properties for design optimization and validating simulation results. Further characterization in dynamic test conditions is essential for final devices to verify their structural integration and performance. Such characterization techniques also help optimize process parameters. Dynamic characterization of the mechanical properties of MEMS structures is a challenging task. In this review article we present our work on the application of inline DHM for MEMS device inspection and complete characterization. The potential use of DH based microscopy system shows promising applications for MEMS device characterization.²³⁻²⁶ The main limitation of current DH based systems is because of stand-alone bulky optical systems need the samples to be brought to the measurement stage. To this end this article also presents a simple, compact (hand held) and powerful DH based lensless microscopy system developed by the authors for MEMS characterization. The proposed system is based on the incorporation of lensless magnification with DH to provide a compact system suitable precisely to fulfill the MEMS devices measurement requirements.

This manuscript has been divided into the following sections. Section II describes the digital recording and reconstruction methods employed for MEMS characterization. In Section III, DHM system development and numerical methodologies for 3D imaging, static and dynamic measurements are described. Further, a handheld DHM system developed by authors is presented. Section IV describes the characterization methodologies and in Section V, results from the characterization of various MEMS devices are shown and discussed. This section is divided into static, dynamic and thermal load characterization. Finally, summary and perspectives are given in Section VI.

2 Digital Hologram Recording and Reconstruction

2.1 Digital hologram recording

The interference of the reference beam and the object beam is recorded by a CCD sensor which is placed in the Fresnel diffraction region of the object wave. The collimated reference beam is incident normally on the CCD and θ is the offset angle of the object as shown in Fig. 1. For efficient utilization of the recording sensor, it is important that the sampling theorem must be fulfilled across its entire CCD sensing area. Thus, for a certain lateral

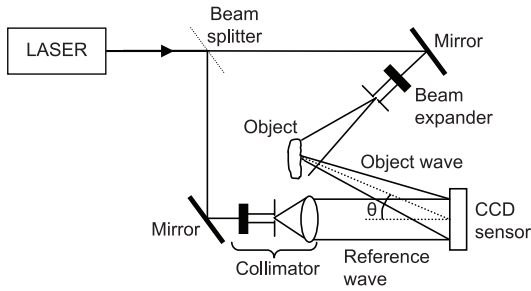


Figure 1: Digital Fresnel holography set-up.

size of the object, the recording distance (between object and CCD sensor) should be greater than a particular minimum value. The limited resolution of CCD sensors limits the angle θ (called interference angle) between the object and reference beams to few degrees only. For exact recovery of the object information during reconstruction process, the sampling theorem requires that the interference fringe spacing must be larger than the size of two pixels of CCD, i.e.

$$\theta < \frac{\lambda}{2\Delta_x} \quad (1)$$

where λ is the wavelength of light used and Δ_x is the pixel size of the CCD. The recording distance, between the object and CCD, is an important parameter to control the interference angle.

During the interference of object and reference beams the waves propagate along the same optical axis. Consider (x, y) to be the hologram plane and the object and reference waves denoted by $O(n_x, n_y)$ and $R(n_x, n_y)$ at the CCD plane. Here $n_x = 0, 1, \dots, N_x - 1$ and $n_y = 0, 1, \dots, N_y - 1$ are the pixel indices of the camera, and $N_x \times N_y$ is the size of the CCD sensor in pixels. The hologram is the interference of the object and reference waves, and can be written as,

$$\begin{aligned} h(n_x, n_y) &= |O(n_x, n_y) + R(n_x, n_y)|^2 \\ &= |O(n_x, n_y)|^2 + |R(n_x, n_y)|^2 \\ &\quad + O^*(n_x, n_y)R(n_x, n_y) \\ &\quad + O(n_x, n_y)R^*(n_x, n_y) \end{aligned} \quad (2)$$

Here O^* and R^* are the complex conjugate of O and R , respectively. The CCD, placed at the hologram plane, records the interference pattern as given in Eqn. 2. For digital recording, the sampling theorem requires that the interference fringe spacing must be larger than the size of two pixels of CCD. The recorded pattern is converted

into a two-dimensional array of discrete signals by using the sampling theorem. Let pixel size of the CCD be Δ_x and Δ_y , then the digitally sampled holograms can be written as,

$$\begin{aligned} H(n_x, n_y) &= \left[h(n_x, n_y) \otimes \text{rect} \left(\frac{x}{\alpha\Delta_x}, \frac{y}{\beta\Delta_y} \right) \right] \\ &\times \text{rect} \left(\frac{x}{N_x\Delta_x}, \frac{y}{N_y\Delta_y} \right) \text{comb} \left(\frac{x}{\Delta_x}, \frac{y}{\Delta_y} \right) \end{aligned} \quad (3)$$

where \otimes represents the two-dimensional convolution and $(\alpha, \beta) \in [0, 1]$ are the fill factors of the CCD pixels.

2.2 Numerical reconstruction methods

The reconstruction of hologram is a diffraction process. The diffraction geometry is shown in Fig. 2.

Numerical reconstruction of hologram is performed using the Fresnel diffraction theory. The hologram $H(n_x, n_y)$, recorded at (ξ, η) plane, is multiplied by the numerical reconstruction wave $R(n_x, n_y)$ and the numerically reconstructed wave-field $U(n'_x, n'_y)$, at the image plane (x', y') , at distance d' from the hologram plane is given by the Fresnel diffraction equation,²⁷

$$\begin{aligned} U(n'_x, n'_y) &= \frac{e^{ikd'}}{i\lambda d'} \int_{-\infty}^{\infty} \int_{-\infty}^{\infty} H(n_x, n_y) R(n_x, n_y) \\ &\times \exp \left[\frac{i\pi}{\lambda d'} \{ (x' - \xi)^2 + (y' - \eta)^2 \} \right] d\xi d\eta \end{aligned} \quad (4)$$

where $k = \frac{2\pi}{\lambda}$, is the wave number.

2.2.1 Fresnel transform method: The impulse response $g(n_x, n_y)$ of the coherent optical system can be defined as

$$g(n_x, n_y) = \frac{e^{ikd'}}{i\lambda d'} \exp \left\{ \frac{i\pi}{\lambda d'} (\xi^2 + \eta^2) \right\} \quad (5)$$

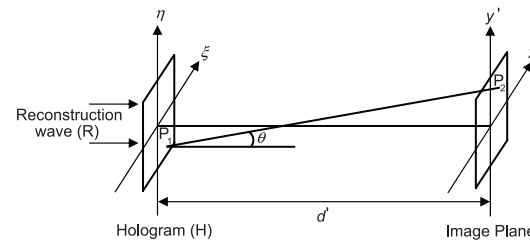


Figure 2: Diffraction geometry of hologram reconstruction.

Using Equation (4), Equation (5) can also be written as

$$U(n'_x, n'_y) = e^{i\pi d'(\nu^2 + \mu^2)} \int_{-\infty}^{\infty} \int_{-\infty}^{\infty} H(n_x, n_y) \times R(n_x, n_y) g(n_x, n_y) \times \exp[-2\pi i\{\xi\nu + \eta\mu\}] d\xi d\eta \quad (6)$$

Here $\nu = \frac{x'}{\lambda d'}$ and $\mu = \frac{y'}{\lambda d'}$ are the spatial frequencies present in the hologram. Thus the reconstructed field is simply the Fourier transform of the product of the hologram, the reconstruction wave and the impulse response function. i.e.

$$U(n'_x, n'_y) = \mathfrak{F}\{H(n_x, n_y) \times R(n_x, n_y) g(n_x, n_y)\} \quad (7)$$

If the hologram recorded with CCD contains $N_x \times N_y$ pixels with pixel size Δ_x and Δ_y along the coordinates respectively. Then the reconstructed field defined by Eqn. (7) converted to finite sums as:²

$$U(n'_x, n'_y) = \frac{e^{ikd'} i\pi\lambda d'}{i\lambda d'} e^{\left(\frac{k^2}{N_x^2\Delta_x^2} + \frac{l^2}{N_y^2\Delta_y^2}\right)} \times \sum_{n_x=0}^{N_x-1} \sum_{n_y=0}^{N_y-1} H(n_x, n_y) R(n_x, n_y) e^{\left[\frac{i\pi}{\lambda d'}(n_x^2\Delta_x^2 + n_y^2\Delta_y^2)\right]} e^{\left[-2\pi i\left(\frac{n_x k}{N_x} + \frac{n_y l}{N_y}\right)\right]} \quad (8)$$

where $k = 0, 1, \dots, N_x - 1$ and $l = 0, 1, 2, \dots, N_y - 1$. Equation (8) is the discrete Fresnel transformation. The matrix $U(n'_x, n'_y)$ is the discrete Fourier transform of the product of $H(n_x, n_y)$,

2.2.2 Convolution method: Reconstruction by convolution approach is useful if the pitch of the reconstructed image has to be independent of the reconstruction distance. It can be shown that the diffraction integral (Eqn. (6)) becomes a convolution for a linear space invariant system. Then the numerically reconstructed wavefield can be written as,

$$U(n'_x, n'_y) = [H(n_x, n_y) R(n_x, n_y)] \otimes [g(n_x, n_y)]$$

here, \otimes indicates a two dimensional convolution. The reconstructed wavefield can be calculated by using the convolution theorem,

$$U(n'_x, n'_y) = \mathfrak{S}^{-1}[\mathfrak{F}\{H(n_x, n_y) R(n_x, n_y)\} \mathfrak{F}\{g(n_x, n_y)\}] \quad (10)$$

The calculation of the Fourier transforms can be performed effectively by the FFT algorithm. The Fourier transform of the impulse

response is called the transfer function $G(n, m)$ of free space propagation and numerically defined as,²

$$G(n_x, n_y) = \exp\left\{\frac{2\pi i d'}{\lambda} \sqrt{1 - \frac{\lambda^2(n_x + N_x^2\Delta_x^2/2d'\lambda)^2}{N_x^2\Delta_x^2} - \frac{\lambda^2(n_y + N_y^2\Delta_y^2/2d'\lambda)^2}{N_y^2\Delta_y^2}}\right\} \quad (11)$$

$R(n_x, n_y)$ and $\exp\{(i\pi/\lambda d')(m^2\Delta_x^2 + n^2\Delta_y^2)\}$. Thus calculation of reconstructed wavefield can be done effectively by using the fast Fourier transform (FFT) algorithm. The pixel size of the numerically reconstructed image varies with the reconstruction distance and is given by,

$$\Delta'_x = \frac{\lambda d'}{N_x \Delta_x}, \quad \Delta'_y = \frac{\lambda d'}{N_y \Delta_y} \quad (9)$$

Then the reconstructed wavefield is given by,

$$U(n'_x, n'_y) = \mathfrak{S}^{-1}[\mathfrak{F}\{H(n_x, n_y) R(n_x, n_y)\} G\{n_x, n_y\}] \quad (12)$$

The pixel size of the reconstructed image by convolution method is same as the pixel size of CCD and does not vary with reconstruction distance, i.e. $\Delta'_x = \Delta_x$ and $\Delta'_y = \Delta_y$.

The Fresnel approach of reconstruction (Eqn. (7)) is fast and useful when the object is larger than the CCD, but variation of pixel size with reconstruction distance creates problems in application such as particles sizing and colour holography. The pixel size of the reconstructed image remains constant with reconstruction distance in convolution approach but it is used when the object size is smaller than the CCD. In case of large sized object, zero padding of holograms is necessary before reconstruction by convolution method.

The image intensity I and phase ϕ at the real image plane can be calculated by,

$$I = |U(n_x', n_y')|^2 \quad \text{and} \\ \phi = \arctan[\text{Im}(U(n_x', n_y'))/\text{Re}(U(n_x', n_y'))] \quad (13)$$

where Re denotes the real part and Im the imaginary part.

3 DHM System Development for MEMS Characterization

3.1 In-line based DHM system

For recording digital holograms different optical configurations have been reported in literature depending on the application, object condition, phase information and reconstruction methods. In this article we focus on inline reflection and lensless reflection DHM systems. An optical arrangement of the in-line digital holographic microscopy system is shown in Fig. 3. A cw laser beam (He-Ne laser 632 nm or DPSS-532 nm) is divided into two parts and intensities of the beams are adjusted to maximize the contrast of the interference fringes. A long distance microscope (LDM) is used in the object beam path to magnify the object micro-features. The magnified object beam interferes with the in-line reference beam after combining, using a cube beam-splitter and then recorded numerically using a CCD sensor and stored in a computer for further digital image-processing.

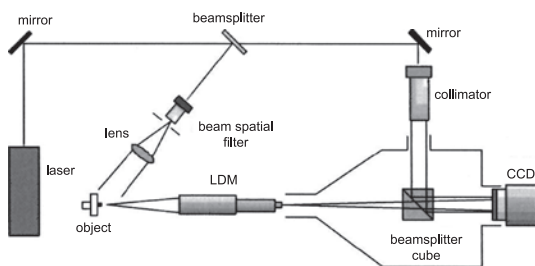


Figure 3: In-line digital holographic microscope set-up.²⁸

3.2 Lens-less in-line DHM system

The reflection type lensless DH microscopic system geometry is shown in Fig. 4. A diverging laser beam from the fiber end provides the magnification in a lensless geometry. The beam is divided into two parts by using a beam splitter; one beam illuminates the sample and other incident on the plane mirror. The sample is illuminated by the diverging beam, coming from the beam splitter. The scattered light from the sample (object beam) is combined with the other diverging beam, reflected from the mirror (reference beam) and the resulting interference pattern is recorded by the CCD. The distance between object and CCD controls the magnification of the system.

3.3 Lensless magnification

DH with collimating object wave provides no magnification. It has two limitations: first is the poor lateral resolution because of the pixel size of available CCD sensors and the second is poor depth resolution for 3D imaging.^{14,29} In order to get magnification without using any lens system and to overcome these problems, a diverging wave can be used in place of the collimated wave to illuminate the object. The concept of diverging wave is shown in Fig. 5. The divergence of the wave provides the geometrical magnification and thus improves the system resolution. At the same time numerical aperture of the system is increased which results in better depth resolution.

This optical system is housed in a compact metal casing (box) as shown in Fig. 6. The illumination source is a single mode optical fiber end which provides the diverging laser beam attached to the casing. The other end of the fiber is attached to the laser. The wavelength of the light is chosen according to the application and/or the required lateral resolution. For the presented system, a fiber coupled laser diode with wavelength 642 nm is used. The diverging beam is delivered from the end of an optical fiber, where the smaller

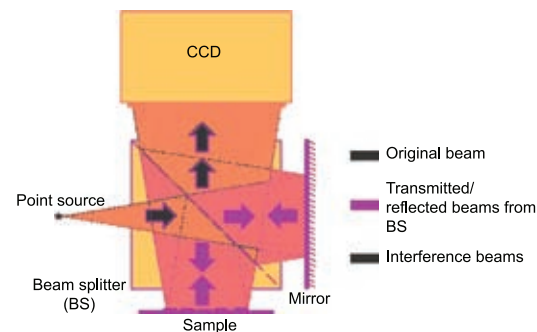


Figure 4: Optical geometry of the lensless DH system.²³

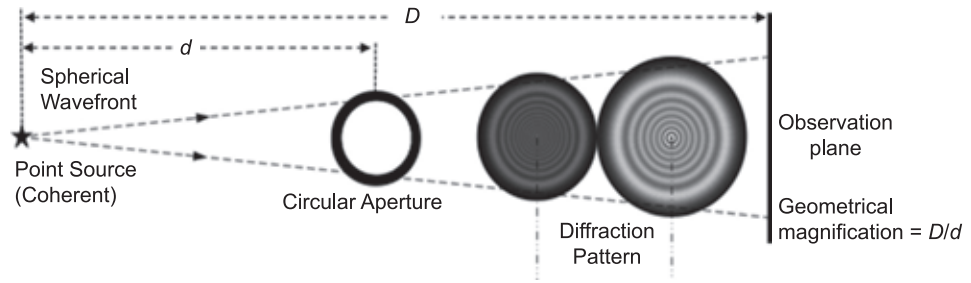


Figure 5: Lensless magnification.



Figure 6: Packaged handheld digital holographic microscopy system.²⁵

the diameter of the fiber (for example in the order of wavelength) the greater the cone of the emitted light coming through it. Therefore, a smaller diameter fiber may increase the Numerical Aperture (NA) of the system and thus the system resolution.

4 Characterization Methodologies

4.1 3D profile measurement

Numerically reconstructed phase information is used to measure the 3D profile of the MEMS samples. The sample height/depth t can be written as:

$$t = \frac{\lambda\phi}{4\pi} \quad (14)$$

Direct phase values can be converted into height/depth values if the measurement is less than half the wavelength of the source used. For larger measurement values, phase unwrapping method is used to remove the phase jumps. In case of steep height measurements of more than half wavelength, the phase jumps cannot be identified accurately and it creates errors in measurements. It is important to note that for direct 3D

profile measurements, we used the off-axis geometry of our DHM system to remove the effect of twin-image wave and zero-order wave from the real-image wave. However, for static and dynamic deformation measurements, we used the in-line geometry of DHM system, and in order to suppress the effect of twin-image and zero-order waves effect interferometric methods are used, as described in the following sections.

4.2 Static and deformation measurements

Static measurement is performed using interferometry method. The instantaneous fast dynamic deformation of sample can also be measured using high speed CCD camera with the system. When a sample surface is illuminated by the laser beam, the light wave reflected from the object surface can be written at the hologram plane as,

$$O(n_{x'}, n_{y'}) = O_0(n_{x'}, n_{y'})e^{i\phi_0(n_{x'}, n_{y'})} \quad (15)$$

where $O_0(n_{x'}, n_{y'})$ is the amplitude of the reflected light and $\phi_0(n_{x'}, n_{y'})$ is the phase that represents the object surface properties. This object wave interferes with the reference wave and hologram is recorded using CCD.

The phase subtraction of the reference state from the deformed state represents the modulo 2π interference phase, which provides the deformation map. Let ϕ_0 be the phase corresponding to the static state of the object (reference state) and ϕ_1 be the phase corresponding to the deformation state, then the subtraction of the phases provides the interference pattern written as,

$$\Delta\phi_{2\pi} = \phi_1 - \phi_0 \quad (16)$$

4.3 Vibration measurements

For a sinusoidally vibrating object, the instantaneous object wave at any instant coming from the vibrating object is defined as,

$$\begin{aligned}
 O'(n_{x'}, n_{y'}, t) \\
 = O_0(n_{x'}, n_{y'}) e^{i\phi_0(n_{x'}, n_{y'})} e^{i[\vec{K} \cdot \vec{z}_v(n_{x'}, n_{y'}, t)]} \quad (17)
 \end{aligned}$$

where $\phi_0(x, y)$ is the phase representing the mean deformation state of the vibrating object, \vec{K} is the sensitivity vector and $\vec{z}_v(x, y)$ is the amplitude of vibration.

Time-averaged method is used to record the hologram. For this method, the frame capture time τ of the CCD should be larger than the period of object vibration. The time averaged object wave is written as,^{30–33}

$$\begin{aligned}
 O(n_{x'}, n_{y'}) &= \frac{1}{\tau} \int_0^\tau O'(n_{x'}, n_{y'}, t) d\tau = O_0(n_{x'}, n_{y'}) \\
 &\quad \times \exp[i\phi(n_{x'}, n_{y'})] \times J_0\{\vec{K} \cdot \vec{z}_v(x, y)\} \quad (18)
 \end{aligned}$$

On numerical reconstruction of time averaged hologram using digital holography system, the reconstructed real image wave is written as,

$$U(n_{x'}, n_{y'}) = O_0(n_{x'}, n_{y'}) e^{i\phi(n_{x'}, n_{y'})} J_0[\vec{K} \cdot \vec{z}_v(n_{x'}, n_{y'})] \quad (19)$$

The amplitude of the numerically reconstructed real image wave is written as follows,

$$\begin{aligned}
 A(n_{x'}, n_{y'}) &= |U(n_{x'}, n_{y'})| \\
 &= O_0(n_{x'}, n_{y'}) J_0\{\vec{K} \cdot \vec{z}_v(n_{x'}, n_{y'})\} \quad (20)
 \end{aligned}$$

and the phase is,

$$\begin{aligned}
 \phi(n_{x'}, n_{y'}) &= \arctan \frac{\text{Im}(U(n_{x'}, n_{y'}))}{\text{Re}(U(n_{x'}, n_{y'}))} \\
 &= \phi_0(n_{x'}, n_{y'}) + \phi_f(n_{x'}, n_{y'}) \quad (21)
 \end{aligned}$$

Here amplitude is modulated by the zero-order Bessel function which provides the information on the mode shape and amplitude of vibrations of the object. The numerically reconstructed phase from time-average hologram is a combination of phase due to mean static state information ϕ_0 , and the time average phase ϕ_f . ϕ_0 varies from $-\pi$ to $+\pi$, whereas ϕ_f is the binary phase (with values 0 and $\pm\pi$) that changes at the zeros of the Bessel function. However, in the presence of both static deformation and vibrations, the phase of

time averaged hologram represents the mixing of the mean deformation and the time-averaged fringes represented by the reconstructed phase information.

5 Applications of DHM in MEMS Device Characterization

5.1 Numerical phase and 3D measurements

First we have explored the technique to inspect the semiconductor wafer warpage. In Fig. 7. a semiconductor device whose surface shows warpage and is detached from the adhesive bond was inspected.^{34,35} The recorded hologram is shown in Fig. 7(a), the reconstructed phase image is shown in Fig. 7(b) which shows the modulo -2π phase which can be further seen clearly in Fig. 7(c). To reconstruct the 3D map from unwrap phase, the phase unwrapping is done and shown in Fig. 7(d)–(e). The warpage revealed by the unwrapped phase image is shown in the 3D representation in Fig. 7(f).

5.2 MEMS and microsystems characterization

5.2.1 Surface profile and 3D measurements of micro-diaphragm: 3D profile measurements of MEMS circular micro-diaphragm are carried out using the quantitative phase information obtained from digital holographic microscope. The diaphragm was fabricated by bonding a piezoelectric plate onto a SOI (silicon on insulator) wafer with 20 μm thick device layer. The thickness of the piezoelectric layer was thinned down to about 40 μm by using chemical/mechanical polish. The back side silicon was etched away by deep reactive ion etching. The hologram of the sample is recorded (Fig. 8.a) using the optical system as shown Fig. 4. The reconstructed amplitude contrast and phase contrast images of the diaphragm are shown in Fig. 8 (b) and (c) respectively. The phase contrast image is significantly different from the amplitude image and is used to measure the surface profile of the diaphragm. The unwrapped phase can be seen clearly in Fig. 8(d) because of the phase jumps of more than 2π . Fig. 8(e) shows 3D map of the unwrapped phase image, and the quantitative value of the phase was converted to a length scale. To calculate the deviation of the diaphragm the line profile is plotted across the diameter of the unwrapped phase contrast image and is shown in Fig. 8(f). It is important to note that the amplitude, phase and 3D profile of the sample is obtained from a single hologram. The developed software provides a near real time reconstruction. Thus, this system

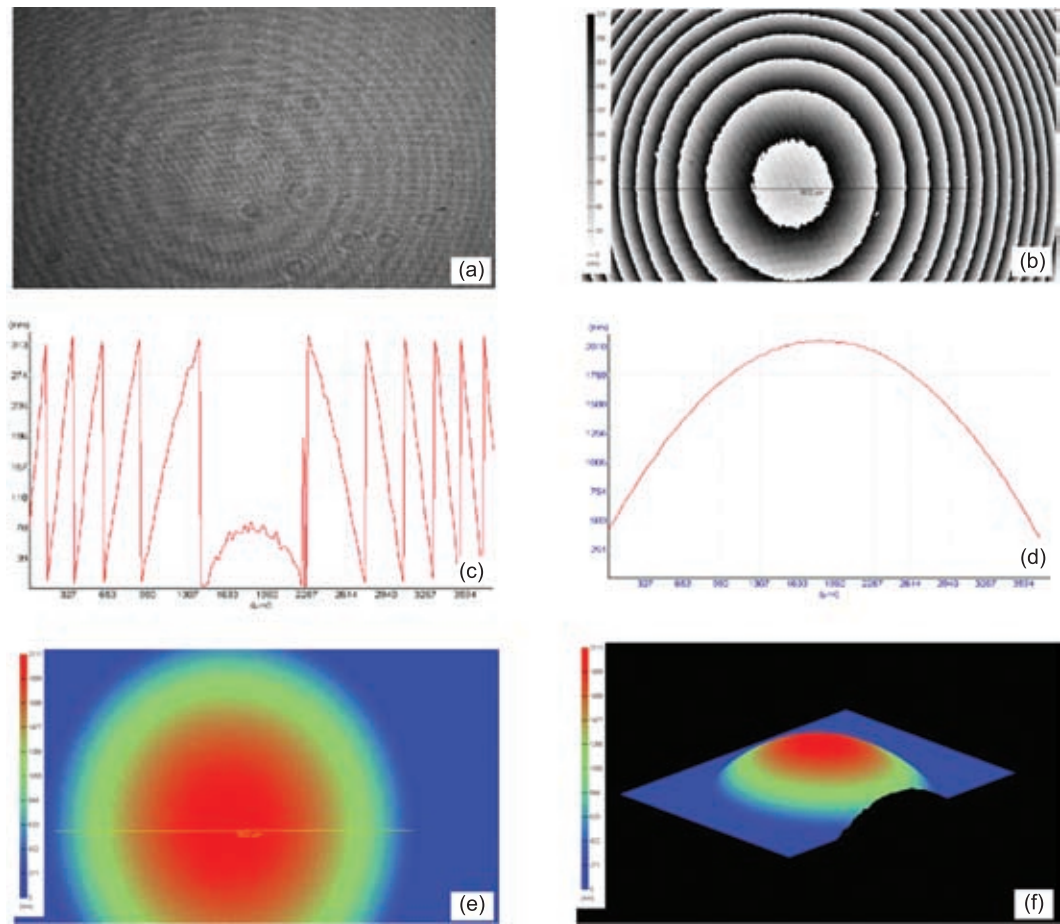


Figure 7: Semiconductor wafer warpage (a) Digital hologram, (b) Wrapped phase profile (c) Modulo- 2π phase image (d) Surface profile (e) Unwrapped phase image (f) 3D perspective.^{34,35}

is useful for the full field fast 3D measurement of MEMS sample surfaces.

5.2.2 Cantilever and microheater device inspection: The application of lensless DH system is presented here for MEMS cantilevers ($300\ \mu\text{m} \times 50\ \mu\text{m}$) on silicon fabricated using aluminium nitride (AlN) patterning³⁶ and thermo-mechanical characterization of microheaters ($140\ \mu\text{m} \times 140\ \mu\text{m}$) fabricated through PolyMUMPs three-layer polysilicon surface micromachining process, and is subjected to a high thermal load.^{37,38} Microheaters are basically resistive beams which can attain a temperature of $300\text{--}400^\circ\text{C}$ due to joule heating, when sufficient voltage is applied across them. The design of microheaters is optimized for low power consumption, low thermal mass, better temperature uniformity across the device and enhanced thermal isolation from the surroundings. Fig. 9 shows the conventional optical microscope (50x) and the DH microscope (numerically reconstructed amplitude image of the hologram) images of the array of cantilevers

and a single microheater chip. It is clear from the Fig. 9 that DHM images are matching with optical microscope images with similar resolution.

5.2.3 Accelerometer device inspection: The performance of a MEMS accelerometer when mounted on two different substrates, ceramic and PCB is tested due to concerns of cracking at the interface of the device and the PCB substrate.²⁶ The surface profile of the device after packaging is studied for both the cases and shown in Fig. 10. Fig. 10(a) and (b) show the phase image and its 3D map of the device when mounted on a ceramic substrate and Figs. 10(c) and (d) are for PCB substrate respectively. It can be clearly seen that the 3D surface map is flat for ceramic substrate while that for the PCM substrate is warped suggesting the introduction of mechanical stress at the interface between device and substrate. This study reveals the importance of the substrate on the characteristics of the MEMS device. Indeed, the warping of the device when mounted on a PCB substrate was a possible reason for damage of this system as compared to the ceramic substrate.

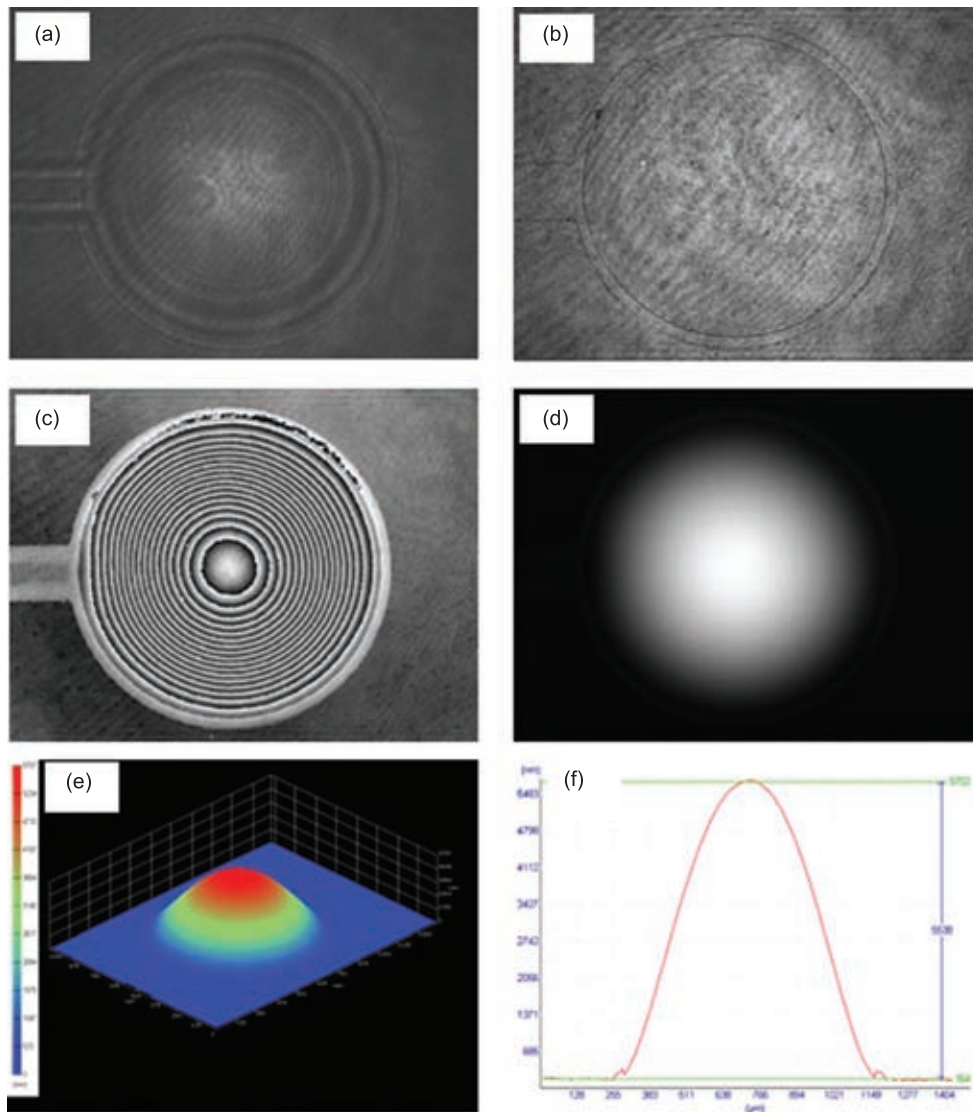


Figure 8: (a) Digital hologram of micro-diaphragm, (b) Reconstructed amplitude image, (c) Reconstructed phase image, (d) Unwrapped phase image, (e) 3D profile of unwrapped phase, and (f) Line profile.^{35,36}

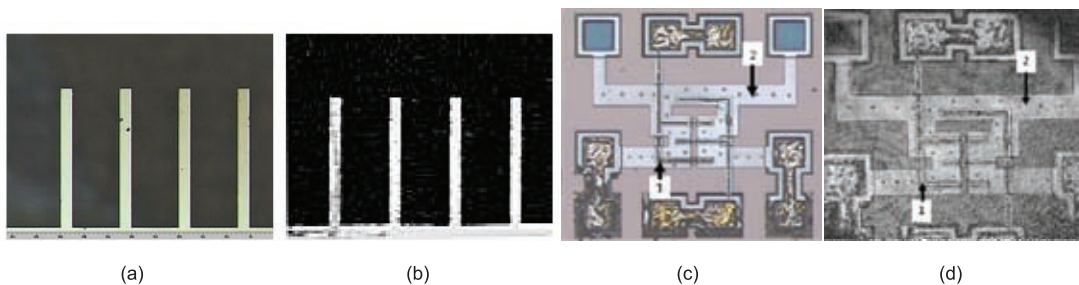


Figure 9: Optical microscopic images (a) and (c), numerically reconstructed digital holographic images (b) and (d) of cantilever and microheater structures respectively.^{36–38}

5.3 Static and dynamic measurements

5.3.1 Deflection measurements of MEMS cantilevers: Aluminium nitride (AlN) films have piezoelectric properties, and represent an alternative

to PZT films. Out-of-plane static deflection analysis of the AlN cantilevers ($300\ \mu\text{m} \times 50\ \mu\text{m}$) is performed using the DHM system.³⁶ The experimental

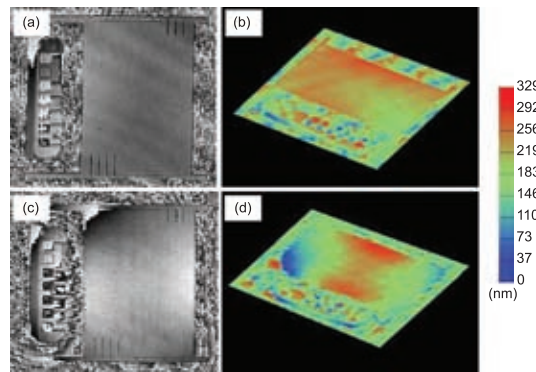


Figure 10: Accelerometer device analysis, (a) and (b) phase image and 3D profile of sensing area for ceramic substrate, and (c) and (d) phase image and 3D profile of sensing area for PCB substrate.²⁶

set-up shown in Fig. 4 is used for deformation study of the cantilevers. The upper and lower electrodes are connected to the power supply, and holograms are recorded corresponding to different applied voltages between the electrodes. The phase information is reconstructed of the recorded hologram recorded at different voltages. The subtraction of the phases, as defined in Eqn. 16, of the deformed state (corresponding to the applied voltage) and reference state (without applying voltage) provides the deformation fringes. Figs. 11(a) & (c) show the

deformation fringes for the two different voltages. Variation in fringe density due to different level of deformation with two applied voltage is clearly observed in the DH phase image. The deformation profile along the length of middle cantilever is plotted in Figs. 11(b) & (d) respectively. This kind of analysis is only possible with DHM and is useful to study of different parts of same device simultaneously corresponding for the same input conditions.

5.3.2 Deformation measurements on MEMS microheaters:

The experimental set-up shown in Fig. 4 is used for thermal deformation study of the micro-heater.²⁶ The electrodes are connected to the power supply, and a series of holograms are recorded corresponding to the different voltages between the electrodes. The hologram of the same sample is recorded, and the numerically reconstructed amplitude image of the hologram is shown in Fig. 9(d). Two points on different electrodes of micro heater as shown in Fig. 9(c) are used to calculate the thermal deformation value at different voltages. For dynamic thermal deformation measurements, the numerical reconstruction of the hologram is performed. The holograms are recorded by varying voltages from 1 volt to 10 volts. The phase information is reconstructed corresponding to the each state. The subtraction

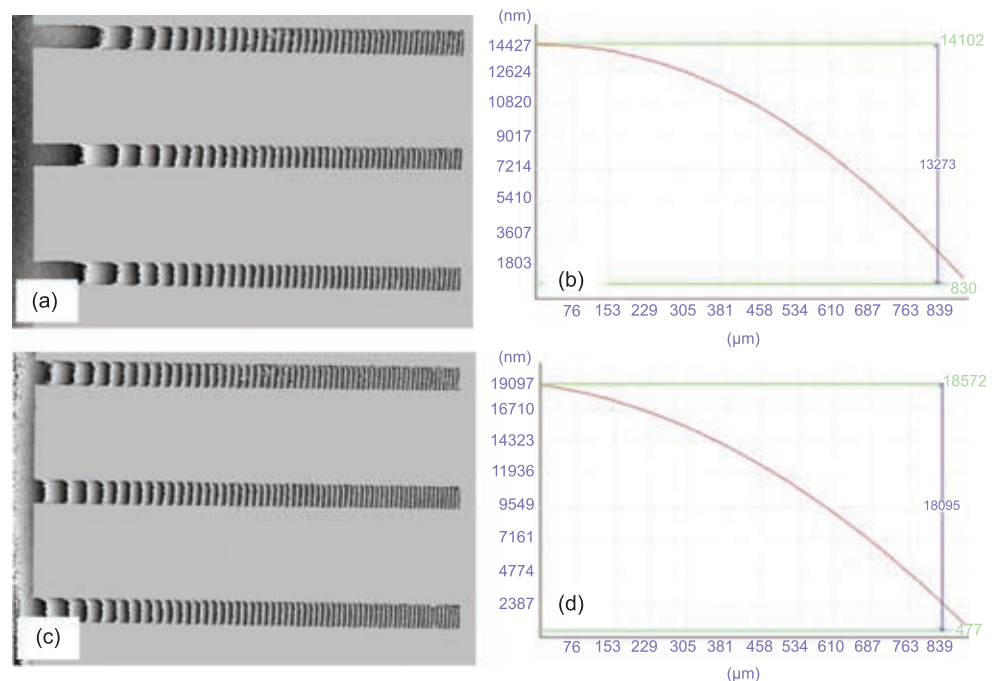


Figure 11: Static deflection measurements in cantilevers (a) & (c) phase subtracted image from the reference state at different applied voltages, and deformation profile of centre cantilevers are shown in (b) & (d) respectively.³⁶

of the phases of the deformed state (corresponding to the applied voltage) and reference state (without applying voltage) provides the deformation fringes. Fig. 12 (a)–(l), shows the deformation fringes for the voltage changes from 1.0 volts to 3.7 volts. Deformation fringes can be clearly observed in the electrodes. It is observed that the number of fringes increases with increase in the voltage, which shows the increase in the thermal deformation with applied voltages.

The deformation fringes corresponding to the higher voltages are shown in Fig. 13 (a)–(l), corresponding to the voltages varying from 7.0 volts to 9.7 volts. The number of fringes in the electrode is large, which shows the higher thermal deformation. It can be also observed that the deformation fringes are also expended in the other electrodes, and increases with increase in temperature. It is an indication of the full field thermal deformation in the device at higher voltages. Thus, this kind of

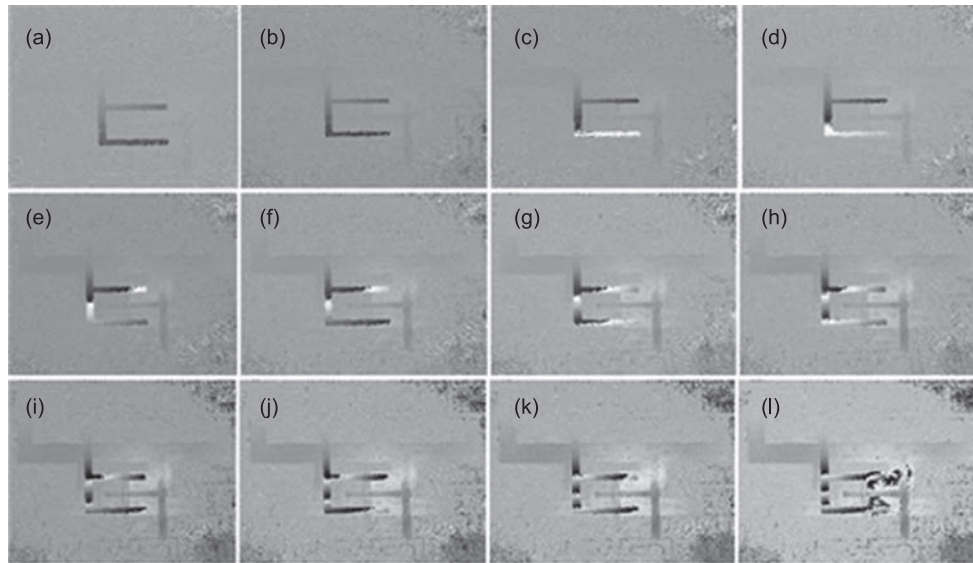


Figure 12: (a) Thermal deformation profile in MEMS micro-heater at applied voltages (a) 1.0 V, (b) 1.25 V, (c) 1.5 V, (d) 1.75 V, (e) 2.0 V, (f) 2.25 V, (g) 2.5 V, (h) 2.75 V, (i) 3.0 V, (j) 3.25 V, (k) 3.5 V, and (l) 3.75 V.³⁸

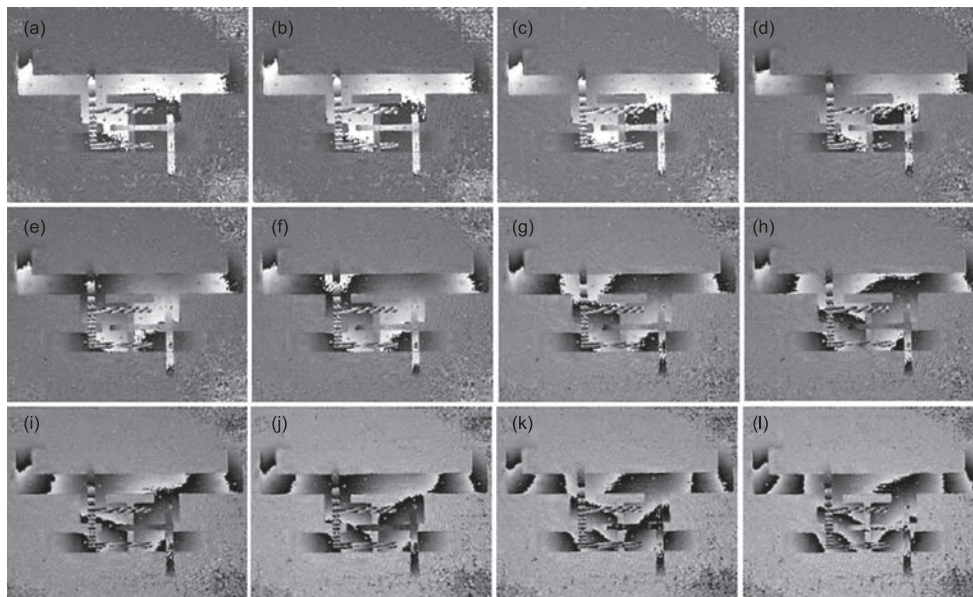


Figure 13: (a) Thermal deformation profile in MEMS micro-heater at applied voltages (a) 7.0 V, (b) 7.25 V, (c) 7.5 V, (d) 7.75 V, (e) 8.0 V, (f) 8.25 V, (g) 8.5 V, (h) 8.75 V, (i) 9.0 V, (j) 9.25 V, (k) 9.5 V, and (l) 9.75 V.³⁸

analysis is particularly useful for full field study of smaller devices, where different components of the device showing different deformations behavior, subject to the same input conditions.

The structural deformation due to thermal stress is quantitatively obtained from the phase analysis of hologram fringes. The vertical deformation is measured at two points: one on the electrode, and the other on the microheater, as indicated in Fig. 9(c). The amplitude of deformation at the applied voltage can be calculated from the obtained fringe patterns shown in Figs. 12 and 13. To do this, the phase difference value is converted into the path difference which represents the vertical deformation. Since an 8 bit CCD sensor is used for recording the hologram and the wavelength of a source is 632.8 nm, it provides a theoretical vertical measurement accuracy of about 2.5 nm.³⁸ The experimentally obtained deformations for the microheater and the electrode, as a function of applied power are compared with the analytically calculated deformations of the doubly clamped beam (at the centre of the beam) and cantilever beam is shown in Fig. 14. It is observed that the analytically obtained values closely match the experimentally observed deformations. As the electrode has a much lower spring constant (0.249 Nm^{-1}) compared to the microheater structure (2.44 Nm^{-1}), the vertical deflection of the electrode is much higher than the microheater. Proposed DHM analysis is very useful in studying the response of different parts of the same micro-device simultaneously, for the same input conditions, and the method can be applied to characterize the MEMS structures. Thus, the proposed characterization of MEMS-based microdevices is

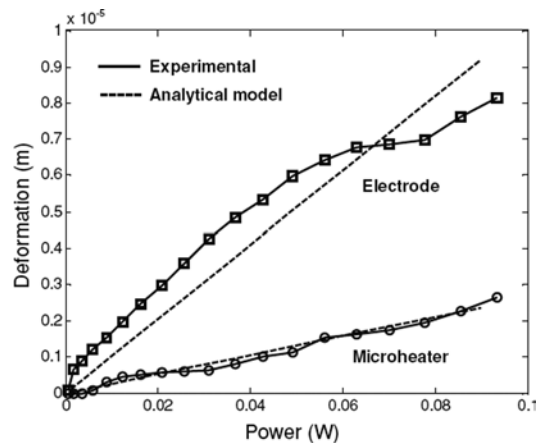


Figure 14: Experimentally measured and analytically computed thermal deformation with varying power at two different points on the device: (1) on the top electrode, and (2) on the microheater.³⁸

useful in inferring the residual stress inside the structure. Analysis of a deformation profile under operating conditions using a non-destructive approach is useful in evaluating the effect of a heating cycle on the structure and the effect of a fabrication process on the final behaviour of the MEMS structures in order to ensure a reliable fabrication of the MEMS. The proposed method can also be extended to measure the non-periodic deformation. In particular, applying this method of characterization, it is possible to evaluate the deformation profile of the MEMS structures not only under the static condition but also under the dynamic condition by taking a sequence of holograms using a high-speed CMOS camera.

5.4 Vibration analysis

5.4.1 MEMS diaphragm: Vibration analysis of an ellipse shaped MEMS diaphragm with the major and minor axes 7 mm and 6 mm respectively is studied.³⁹ The diaphragm was fabricated by bonding a piezoelectric plate onto a SOI (silicon on insulator) wafer with 20 μm thick device layer. The thickness of the piezoelectric layer was thinned down to about 40 μm by using chemical/mechanical polish. The back side silicon was etched away by deep reactive ion etching. The diaphragm is excited by applying an AC driving voltage across the piezoelectric layer. The digital reflection holography system used to investigate the vibration analysis of the diaphragm. The mode shapes of the vibrating MEMS diaphragm are obtained from the reconstruction of time-averaged in-line holograms recorded corresponding to the resonant frequencies. The amplitude of the reconstructed real image wave, which is modulated by the J_0 function, gives the mode pattern. Fig. 15 shows the vibration modes of the diaphragm corresponding to the resonant frequencies. These patterns can be obtained either by reconstruction of single time average hologram, or by subtraction of holograms in two states at the same frequency.

Time averaged holograms were recorded corresponding to a wide range of applied frequencies. In addition to the frequencies shown in Fig. 15, some additional resonant frequencies are also obtained. The mode shapes corresponding to these resonant frequencies are shown in Figs. 16 (a)–(h).

The amplitude of vibration can be determined from the obtained mode patterns. Eqn. (20) is used for vibration amplitude measurements. Zeros of first order Bessel function are used corresponding to the dark fringes for calculating the amplitude values. The time averaged fringes of the diaphragm by increasing the amplitude values at the resonant frequency 15 kHz is shown in Fig. 17. The vibration

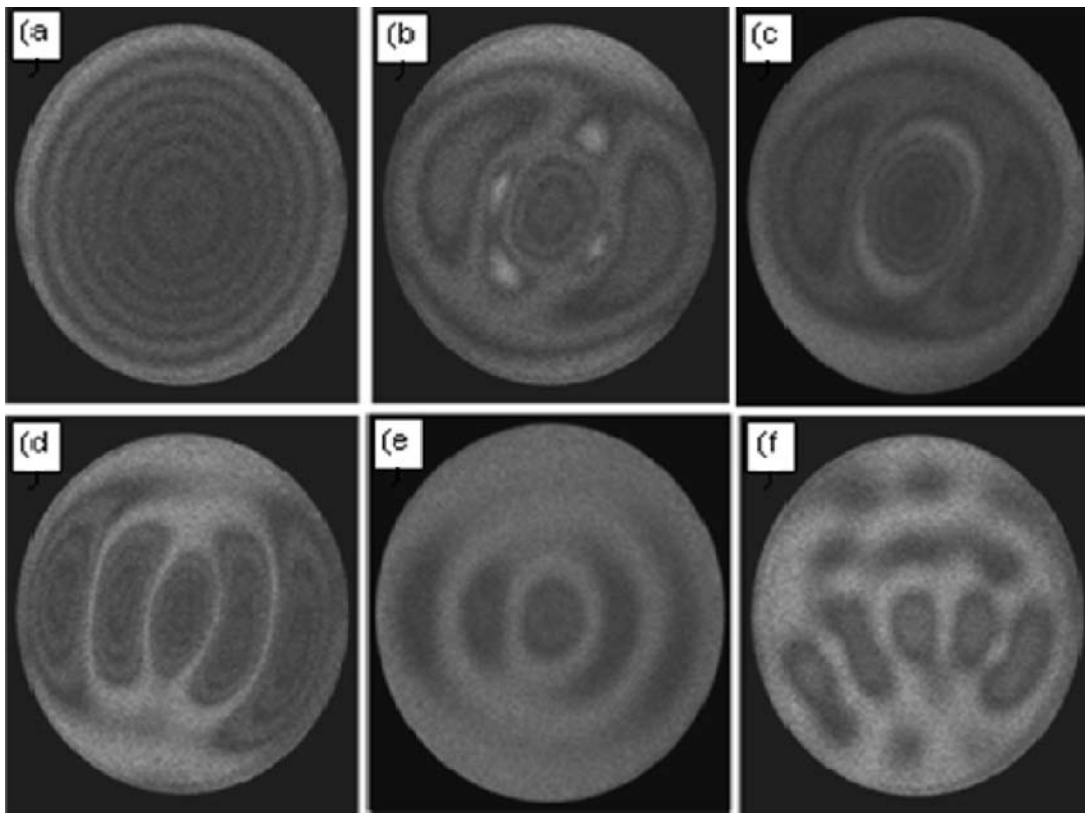


Figure 15: Vibration modes shapes of MEMS diaphragm verifying the frequency spectrum corresponding to the frequencies (a) 12 kHz, (b) 48 kHz, (c) 60 kHz, (d) 120 kHz, (e) 130 kHz, and (f) 143 kHz.³⁹

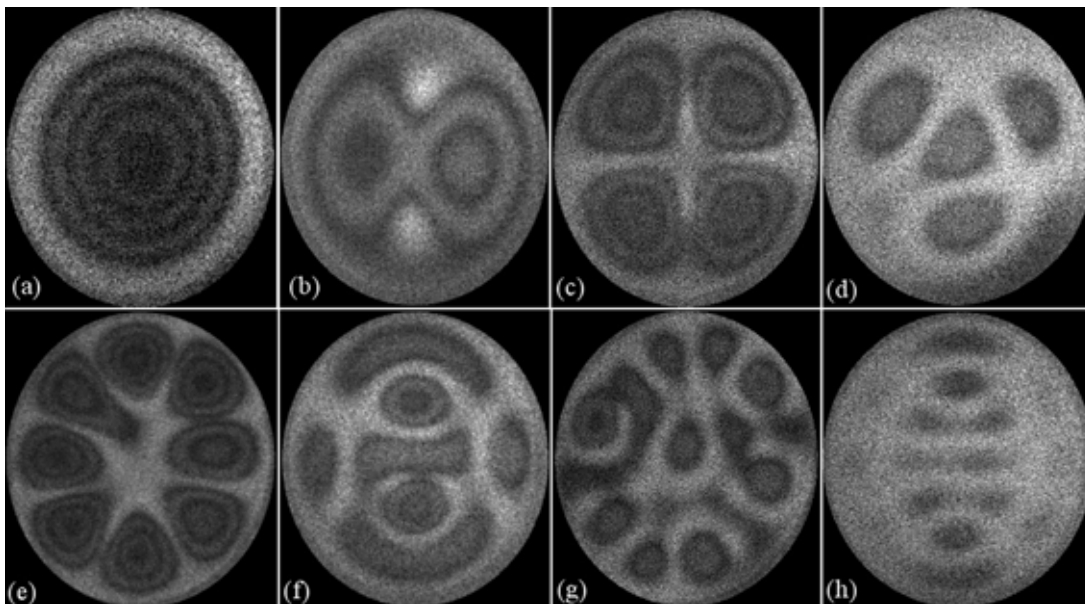


Figure 16: Vibration modes shapes corresponding to the resonant frequencies (a) 14 kHz, (b) 29 kHz, (c) 45 kHz, (d) 70 kHz, (e) 90 kHz, (f) 105 kHz, (g) 145 kHz, and (h) 175 kHz.³³

amplitude values are plotted for different applied voltages and shown in Fig. 18.

The main advantage in using digital holography is to obtain the quantitative phase information of

the reconstructed image wave.³³ As discussed previously, the numerical reconstructed phase from time-averaged holograms contains two parts, the first part represents object surface roughness and

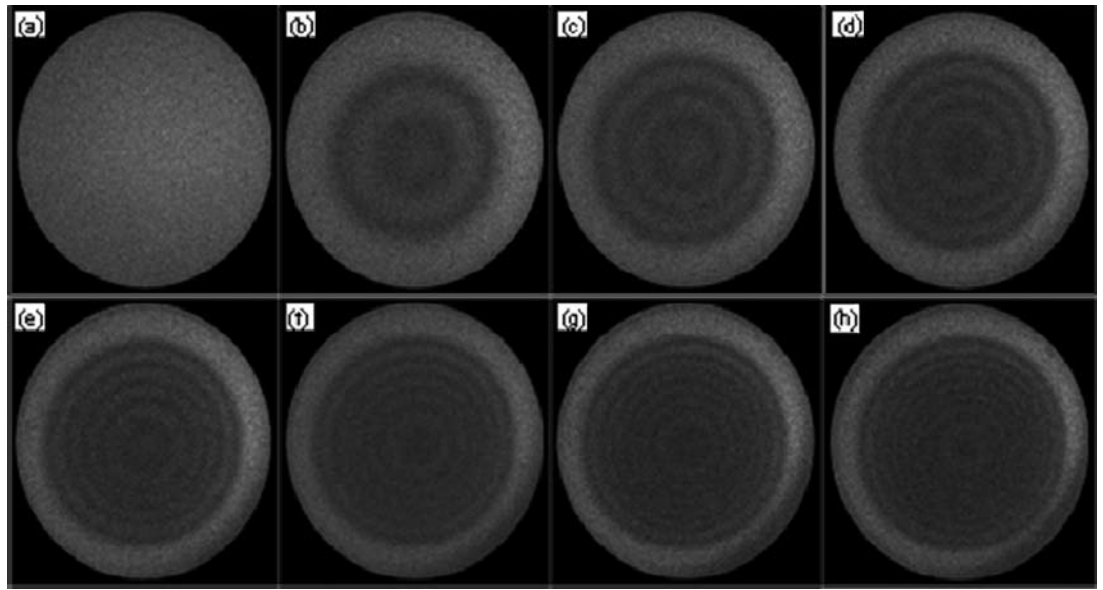


Figure 17: Vibration fringes of MEMS diaphragm as a function of applied voltages (a) 0 V, (b) 1.0 V, (c) 1.5 V, (d) 2.0 V, (e) 2.5 V, (f) 3.0 V, (g) 3.5 V, and (h) 4.0 V.

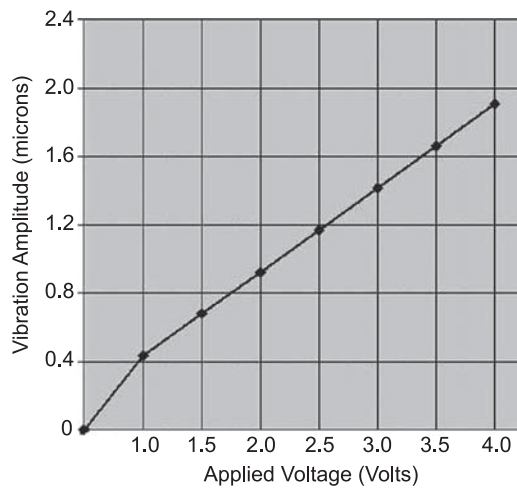


Figure 18: Vibration amplitude variation with applied voltage for MEMS diaphragm.

the second part is called time average phase, which shows the zeros of the J_0 function. For reconstruction of single exposure hologram, the first part of the phase term reconstructs the object surface roughness information. Thus for object with optically rough surfaces, it contributes to the speckle noise. However, in double exposure case, if there is any mean static deformation during vibration amplitude change, the subtraction of the phase term represents the mean deformation. Again for rough object surface the mean deformation fringes occur due to speckle correlation, and for time averaged case the mean static fringes mix with the vibration fringes. For pure sinusoidal

vibration of the object, the subtraction of phases of time average and reference hologram provides only the time average phase. This is shown in Figs. 19 (a)–(c) corresponding to the frequencies (a) 14 kHz, (b) 45 kHz, and (c) 105 kHz. Compared to Fig. 15, all zeros of the J_0 function can be clearly identified from the time average phase. The eventual use of binary jumps is particularly useful in case of higher vibration amplitudes. It is because the time averaged amplitude fringes are modulated by zero-order Bessel function, so for higher order fringes the contrast becomes significantly poor, while the time average phase shows the binary jumps and thus has the same contrast for all orders.

Although the time average phase contains binary values (with numerical values 0 and $\pm \pi$), it provides a clear representation of the zeros of J_0 function; while the simultaneous presence of static phase appears as the speckle noise. The double exposure method cannot completely remove this noise because of the stochastic variations of speckles in the two exposures. This effect can be seen in Fig. 20. In order to explore the mixing of the phase information during phase subtraction, first we have considered the case of pure static deformation, achieved by selecting a non-resonant frequency and applying an off-set voltage to the membrane between exposures. The phase subtraction represents modulo 2π interference phase, same as in conventional digital holographic interferometry. Fig. 20 shows the pure mean static deformation fringes obtained from time averaged

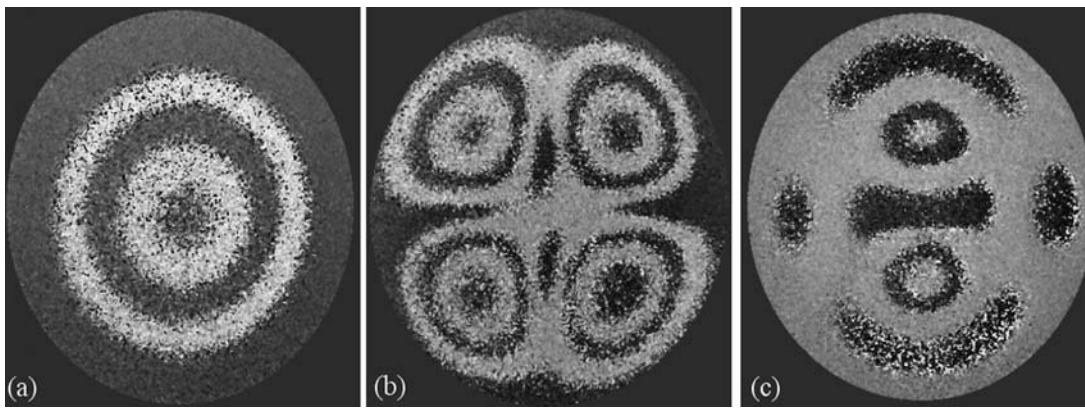


Figure 19: Time average phase representing the binary jumps corresponding to the zero of the Bessel function.³³

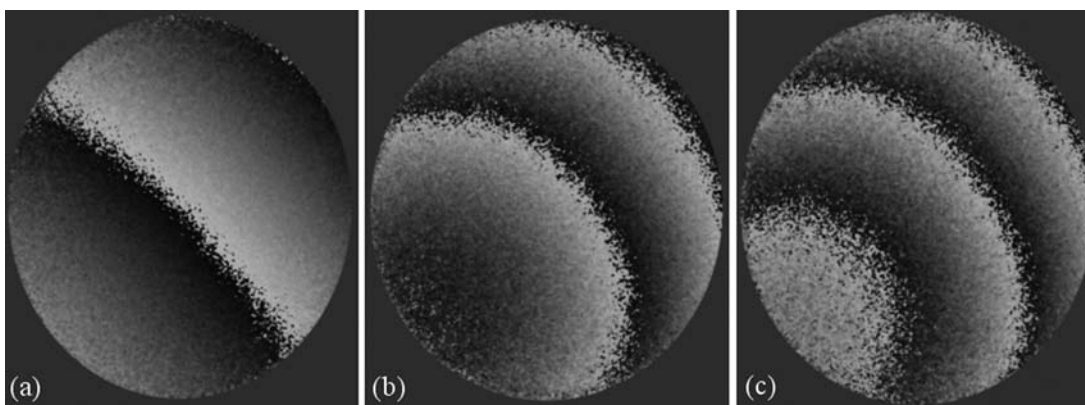


Figure 20: Modulo 2π interference phase representing mean static deformation obtained by applying offset voltage at non resonant frequencies.³³

in-line holograms. The holograms are recorded at a non resonant frequency of 25 kHz, at different voltage with increasing offset voltages (0.5 volt, 1.5 volts and 4.5 volts) applied by the frequency generator.

Mixing of the phase fringes is best visualized when the applied offset voltage excites the membrane in resonance. The mixing shows the cluster of mean deformation and time average phases, which represent the exact vibration behavior of the membrane in the presence of mean static deformations. Thus, the importance of mean static deformation is to study the actual behavior of vibrating objects in the presence of mean static change. Figs. 21 (a)–(c) show the patterns corresponding to the different mean and vibration amplitudes at a resonant frequency of 15 kHz. For double exposure recording, the reference hologram is recorded without vibration, and the time-averaged holograms recorded with driving voltages of 1.0, 1.5, and 2.0 volts and corresponding offset voltages 0.75, 1.5, and 2.5 volts respectively. It can be clearly seen in Fig. 21(a) that the

mean deformation fringe also appears inside the time average phase with a phase jump. This phase jump may be attributed to the balancing condition of the membrane created by the offset voltage. As the offset voltage increases, the number of fringes inside the time average fringe also increases (Figs. 21 (b) and (c)).

5.4.2 Cantilever vibration analysis: Vibration analysis of the aluminium nitride (AlN) cantilevers is performed using the time-averaged digital holographic microscopy system. AlN films have piezoelectric properties, and represent an alternative to PZT films. AlN cantilevers of size $300 \times 50 \mu\text{m}$ long are fabricated using surface micromachining process.^{30,31,36,40} The chip of the MEMS cantilevers device is attached to a standard SD card holder as shown in Fig. 22, which is in turn attached to the frequency generator. The lensless in-line digital holographic microscopy is explored for imaging and dynamic characterization of MEMS cantilevers. The numerically reconstructed image of the three static cantilevers

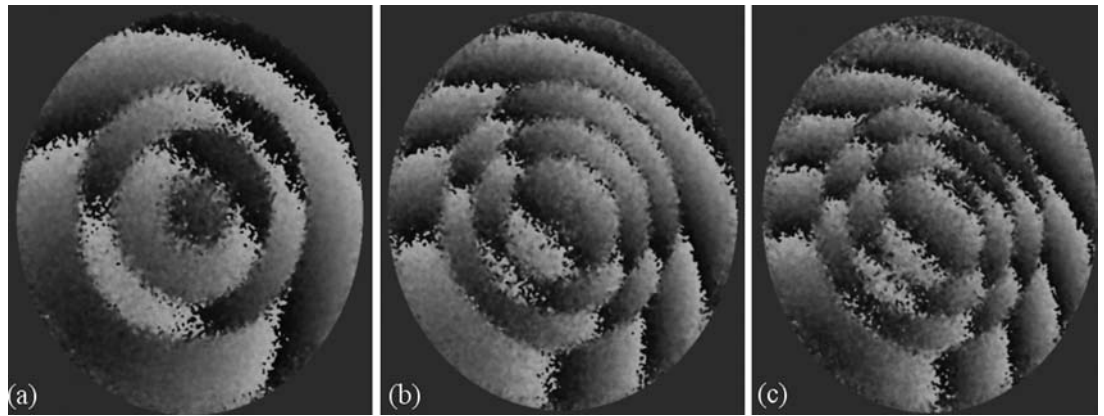


Figure 21: Mixing of mean deformation and time average phases, representing the balancing of the diaphragm in the presence of both vibration and mean deformation.³³

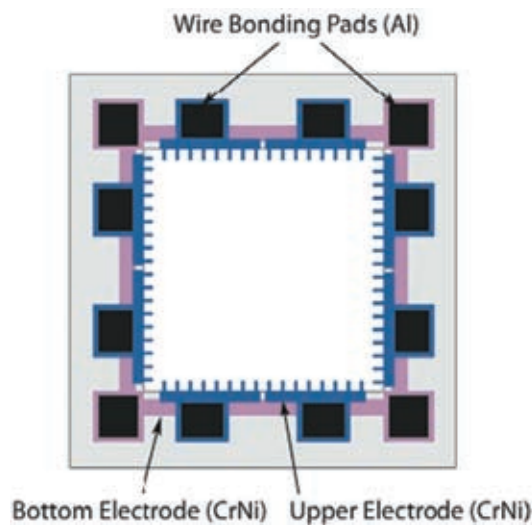


Figure 22: Layout of the $300 \times 50 \mu\text{m}$ long cantilevers. The actuation of the cantilevers is done by applying a voltage between the upper and bottom metal electrodes.³⁹

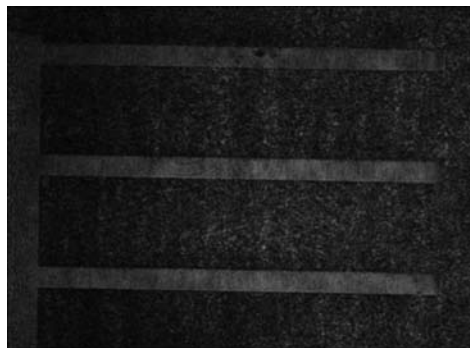


Figure 23: Numerically reconstructed image of cantilevers.³⁰

electronically connected together is shown in Fig. 23 and vibration analysis of these cantilevers is presented here.

The mode shapes of the vibrating cantilevers are obtained from the reconstruction of time-averaged in-line holograms. The amplitude of the reconstructed real image wave, which is modulated by the J_0 function, gives the mode pattern. Time averaged holograms are recorded corresponding to the resonant frequencies of the cantilevers. The mode shapes corresponding to the first, second and third resonant frequencies are shown in Fig. 24, which is obtained by amplitude reconstruction of time-averaged holograms. The vibration modes shown are corresponding to the first, second and third frequencies at (a) 30.46 kHz, (b) 191.40 kHz and (c) 533.0 kHz respectively.

The scanning of frequencies corresponding to the resonant frequencies is performed and amplitudes of all cantilevers are calculated. The zeros of first order Bessel function are used corresponding to the dark fringes for calculating the amplitude values. As it can be clearly seen (Fig. 24) that all the cantilevers are not vibrating at the same resonant frequency. The vibration amplitudes of each cantilever are calculated at each resonant frequency and plotted as shown Fig. 25. The frequency spectrum of cantilevers are shown in Fig. 25(a) and Figs. 25(b)–(d). Fig. 25(b) shows the resonant frequency of the each cantilever corresponding to the first resonant frequency and similarly Figs. 25(c) and (d) show the second and third resonant frequencies respectively.

From the above Figure it is clearly observed that the resonant frequencies of the cantilevers change from higher (right) to lower (left) frequency side. This means in terms of fabrication process these are the cantilevers from edge to centre

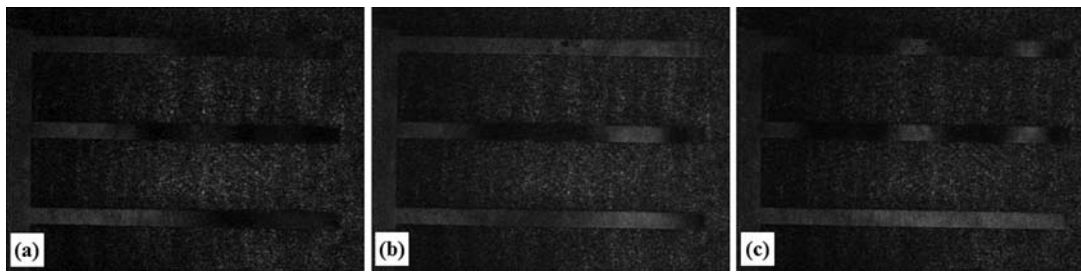


Figure 24: Mode shape corresponding to the resonant frequencies (a) 30.46 kHz, (b) 191.40 kHz, and (c) 533.0 kHz.¹⁹

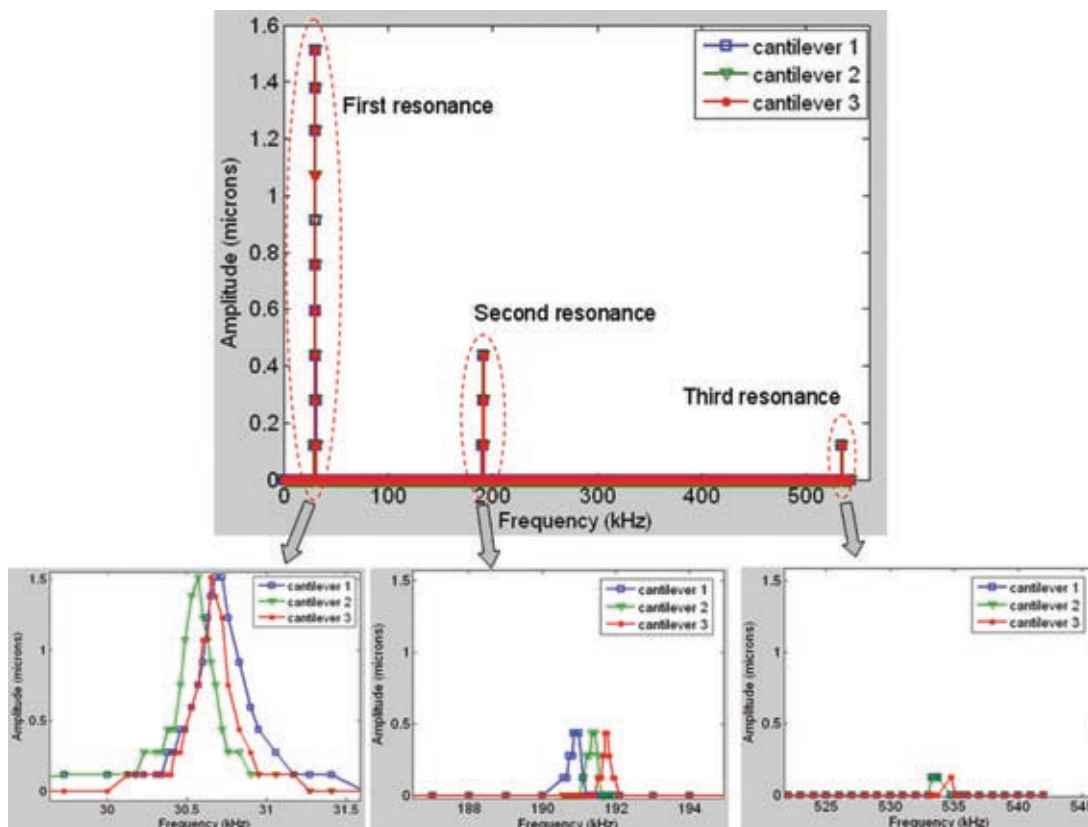


Figure 25: (a) Frequency spectrum of the cantilevers, and resonant frequencies of cantilevers corresponding to (b) First resonant, (c) Second resonant, and (d) Third resonant frequency.³⁰

of the wafer. We suspect that this behavior is because of change in the stiffness coefficient at various location of wafer during fabrication process. Thus a complete dynamic analysis of an array of cantilevers is demonstrated using the DHM system.

6 Summary and Perspectives

In this review article we have presented the recent developments in DHM technique and its applications in MEMS structure and device characterization. Numerical reconstruction methods and their extension for MEMS inspection and

complete characterization are discussed. Development of inline DHM system for complete characterization of MEMS is presented. The numerical methodologies developed for the analysis and its application in static, deformation and dynamic measurements and analysis are demonstrated. The applications of the system are presented for different MEMS device characterization. Static inspection of the semiconductor wafer, MEMS diaphragm, cantilevers and microheater structures are shown. Utility of the develop system in deflection measurement of array of cantilevers

and deformations study of array of micro-heaters under device actuation conditions are demonstrated. Vibration analysis of an array of cantilevers, MEMS diaphragm under different voltages and frequencies using the time-averaged method is discussed. Methodology for deformation analysis under device vibrating conditions is illustrated. The developed system is best suited for full-field and real-time measurement of MEMS and similar microstructure samples for static and dynamic characterization in real time. Proposed DH based microscopic analysis can easily be applied to any MEMS/MOEMS device and other similar microstructures.

This review article has highlighted the DHM applications in MEMS metrology. However, DHM has been successfully applied in wide range of micrometrology applications due to its unique advantages such as: 3-D information extraction with single imaging, phase shift imaging capability, digital autofocusing, no optical aberration correction, low cost etc. as compared conventional optical microscopy. More specifically, due to DHM's capability of non-invasively visualizing and quantifying biological tissue, bio-medical imaging applications have received large share of attention in recent years. Furthermore, DHM's capability in label-free cell counting in adherent cell cultures, label-free viability analysis of adherent cell cultures, label-free morphology analysis of cells, label-free cell cycle analysis and red blood cell analysis has made the system a potential tool in complete bio-imaging and analysis applications.

Received 10 February 2013.

References

1. D. Gabor, "A new microscopic principle", *Nature*, **161**, 777–778, (1948).
2. U. Schnars, and W. Jüptner, "Digital holography and numerical reconstruction of holograms", *Meas. Sci. Tech.*, **13**, R85 (2002).
3. U. Schnars U. and Jüptner W, "Direct recording of holograms by a CCD-target and numerical reconstruction" *Appl. Opt.* **33**, 179–81 (1994).
4. U. Schnars, "Direct phase determination in hologram interferometry with use of digitally recorded holograms" *J. Opt. Soc. Am. A* **11**, 2011–5 (1994).
5. E. Cuhe, F. Bevilacqua and C. Depeursinge, "Digital holography for quantitative phase-contrast imaging", *Opt. Lett.* **24**, 291–3 (1999).
6. C. Wagner, S. Seebacher, W. Osten and W. Jüptner, "Digital recording and numerical reconstruction of lensless Fourier holograms in optical metrology", *Appl. Opt.* **38**, 4812–20 (1999).
7. Myung-K. Kim, "Applications of Digital Holography in Biomedical Microscopy". *J. Opt. Soc. Korea* **14** (2): 77–89(2010).
8. C. Daniel, K. Björn, W. Günther and Gert von Bally, "Parameter-Optimized Digital Holographic Microscope for High-Resolution Living-Cell Analysis". *Appl. Opt.*, **43** (33): 6536–6544 (2004).
9. J. Desse, P. Picart, and P. Tankam, Digital three-color holographic interferometry for flow analysis, *Opt. Expr.* **16**, 5471–5480 (2008).
10. J. Desse, P. Picart, P. Tankam, "Digital color holography applied to fluid and structural mechanics, *Opt. & Las. Eng.*, **50**, 18–28 (2012).
11. C. Fournier, C. Barat, C. Ducottet and T. Fournel, "Digital holography applied to particle image velocimetry", *Proc. PSFVIP-4*. 1–9 (2004).
12. D.D. Aguayo, F.M. Santoyo, M.H. De la Torre-I, M.D. Salas-Araiza, C. Caloca-Mendez and D.A. Gutierrez Hernandez, "Insect wing deformation measurements using high speed digital holographic interferometry", *Opt. Expr.* **18**, 5661–5667 (2010).
13. E. Darakis, T. Khanam, A. Rajendran, V. Kariwala, T.J. Naughton and A. Asundi "Microparticle characterization using digital holography". *Chem. Eng. Sci.* **65** (2): 1037–1044 (2010).
14. V.R. Singh, G.M. Hegde, A. Asundi, "Particle field imaging using digital in-line holography", *Curr. Sci.*, **96** (3): 391 (2009).
15. Tong Zhang, Ichirou Yamaguchi, "Three-dimensional microscopy with phase-shifting digital holography". *Optics Letters* **23** (15): 1221–1223 (1998).
16. *Digital Holography Microscopy applications: "Three Dimensional Object Analysis and Tracking* by Cedric Schockaert, VDM Verlag (2009).
17. Lei Xu, Xiaoyuan Peng, Jianmin Miao and Anand Asundi, "Studies of digital microscopic holography with applications to microstructure testing", *Appl. Opt.*, **40**, 5046 (2001).
18. B. Kemper, D. Carl, J. Schnekenburger, I. Bredebusch, M. Schäfer, W. Domschke and G. von Bally, "Investigations on living pancreas tumor cells by digital holographic Microscopy", *J. Biomed. Opt.* **11**, 034005 (2006).
19. G. Pedrini, S. Schedin and H. Tiziani, "Lensless digital holographic interferometry for the measurement of large objects" *Opt. Commun.* **171**, 29–36 (1999).
20. I. Yamaguchi, J. Kato, S. Ohta and J. Mizuno, "Image formation in phase-shifting digital holography and applications to microscopy" *Appl. Opt.* **40**, 6177–86 (2001).
21. F. Dubois, L. Joannes and J.C. Legros, "Improved three-dimensional imaging with a digital holography microscope with a source of partial spatial coherence" *Appl. Opt.* **38**, 7085–94 (1999).
22. Mark J Madou, "Fundamentals of Microfabrication", CRC-Press, (1998).
23. F. Montfort, Y. Emery, F. Marquet, E. Chucho, N. Asnert, E. Solanas, A. Mehdaoui, A. Ionescu and

- C. Depenursing, "Process engineering and failure analysis of MEMS and MOEMS by digital holographic microscopy (DHM)", *Proc. of SPIE*, **6463**, 6463G, (2007).
24. G. Coppola, P. Ferraro, M. Iodice, S. De Nicola, A. Finizio, and S. Grilli, "A digital holographic microscope for complete characterization of microelectromechanical systems", *Meas. Sci. Technol.*, **15**, 529, (2004).
 25. Digital Holography for MEMS and Microsystem Metrology, Anand Asundi, Wiley, (2011).
 26. A. Asundi and V.R. Singh, "Digital holography for MEMS applications", *Novel Techniques in Microscopy*, OSA Technical Digest, paper JTuA2, (2009).
 27. J.W. Goodman, Introduction to Fourier Optics, McGraw-Hill, New York, (1996).
 28. L. Xu, X. Peng, A. Asundi and J. Miao, "Hybrid holographic microscope for interferometric measurement of microstructures", *Opt. Eng.*, **40**, 2533–2539 (2001).
 29. Vijay Raj Singh, Emmanouil Darakis, Gopalkrishna Hegde and Anand Asundi, "A new methodology for pixel size retention in lensless digital holographic microscopy applied to micro-particles analysis", *J. Opt.(IOP)* **13**, 035704 (2011).
 30. V.R. Singh and A. Asundi, "In-line digital holography for dynamic metrology of MEMS", Invited Paper, *Chi. Opt. Lett.*, Vol. **7** (12), 1117 (2009).
 31. R.L. Powell and K.A. Stetson, "Interferometric vibration analysis by wavefront reconstruction", *J. Opt. Soc. Am.*, **55**, 1593, 1965.
 32. V.R. Singh, G.M. Hegde and A. Asundi, "Digital in-line holography for dynamic micrometrology", *Proc. of SPIE*, **6188**, 618803–1, (2006).
 33. V.R. Singh, J. Miao, Z. Wang, G.M. Hegde and A. Asundi, "Dynamic characterization of MEMS diaphragm using time averaged in-line digital holography", *Opt. Comm.*, **280**, 285, (2007).
 34. O.C. Chee, V.R. Singh, E. Sim and A. Asundi, "Development of simple user-friendly commercial digital holographic microscope", *Proc. of SPIE*, **6912**, 69120V-1, (2008).
 35. V.R. Singh, S. Lui and A. Asundi, "Compact Handheld Digital Holographic Microscopy System Development", *Proc. SPIE*, **7522**, 75224 L, (2009).
 36. V.R. Singh, A. Anderi, C. Gorecki, L. Nieradko and A. Asundi, "Characterization of MEMS cantilevers using lensless digital holographic microscope", *Proc. SPIE*, **6995**, 69950F-1, (2008).
 37. D. Koester, A. Cowen, R. Mahadevan, M. Stonefield and B. Hardy "PolyMUMPs Design Handbook" (Berlin: MEMSCAP) (2003).
 38. B. Jayaraman, V.R. Singh, A. Asundi, N. Bhat and G.M. Hegde "Thermo-mechanical characterization of surface-micromachined microheaters using in-line digital holography", *Meas. Sci. Technol.*, **21**, 1, (2010).
 39. V.R. Singh, "Lensless Inline Digital Holography for Dynamic Applications", Ph.D. Thesis, Nanyang Technological University, Singapore, (2008).
 40. H. Shi, Y. Fu, C. Quan, C.J. Tay and X. He "Vibration measurement of a micro-structure by digital holographic microscopy", *Meas. Sci. Technol.* **20**, 065301–7, (2009).



Gopalkrishna Hegde received his M.Sc and Ph.D. in Physics, all in India. He is currently with the Centre for Nano Science and Engineering, Indian Institute of Science, Bengaluru. He has over 80 publications in international journals and conference proceedings and filed 4 patents. He has presented invited talks/key notes at various institutions and at international conferences. He has been advisory/review/organizing member of many international and national conferences. He has completed many sponsored research projects in Indian and in Singapore. His current research interests are in the areas of photonics, optical sensors, optical flow visualization, biophotonics, nanofabrication and microfluidics.



Dr. Vijay Raj Singh received Master of Technology (M.Tech.) degree in Applied Optics from Indian Institute of Technology (IIT) Delhi, India in 2003, and Ph.D. degree in Optical Science and Engineering from Nanyang Technological University (NTU), Singapore in 2008. His research interests include digital holography, biomedical imaging, image processing, optical metrology, and 3D microscopy. From 2007–2010, his main research works focused on development of digital holographic microscopes as tabletop and handheld systems for MEMS characterization and 3D imaging of live bio-cells. Currently, he is working with Singapore-MIT alliance for Research and Technology (SMART) centre, Singapore and working on developing 3D microscopy systems and image processing methods for tissue imaging applications. He has 2 US patents (1 granted and 1 pending), published 16 peer reviewed research articles in international journals and 22 papers in international conference proceedings.



Anand Asundi (安顺泰) graduated from the Indian Institute of Technology, Bombay with a B.Tech (Civil Engg.) and a M.Tech (Aeronautical Engg.). Subsequently he received his Ph.D. from the State University of New York at Stony Brook. Following a brief tenure at Virginia Tech., he was with the University of Hong Kong from 1983 to 1996 as Professor in the Department of Mechanical Engineering. He is currently Professor in the School of Mechanical and Aerospace Engineering and Director of the Centre for Optical and Laser Engineering at the Nanyang Technological University in Singapore. His current research interests are in Photomechanics, High Resolution Optical Metrology, 3D Imaging, Measurement and Display and bio-chemical Sensing and Imaging. He has published extensively and presented invited seminars/talks at various institutions and at international conferences. He is Editor of Optics and Lasers in Engineering and Fellow of SPIE, the International Society of Optical Engineers and Institution of Engineers, Singapore and member of the Optical Society of America. He is founding chair of the Optics and Photonics Society of Singapore, Asian Committee on Experimental Mechanics and the Asia Pacific Committee on Smart Materials and Nanotechnology. He has organized numerous conferences and served on the Membership, Scholarship/Awards and Presidential Asian Advisory committees of SPIE and on the Board of Directors of SPIE.